www.czasopisma.pan.pl   PAN   www.journals.pan.pl
POLSKA AKADEMIA NAUK

VERSITA

Stability relationships of REE-bearing phosphates in an alkali-rich system (nepheline syenite from the Mariupol Massif, SE Ukraine)

MAGDALENA DUMAŃSKA-SŁOWIK[1], BARTOSZ BUDZYŃ[2], WIESŁAW HEFLIK[1]
AND MAGDALENA SIKORSKA[3]

[1]*AGH University of Science and Technology, Faculty of Geology, Geophysics and Environmental Protection
Department of Mineralogy, Petrography and Geochemistry, al. A. Mickiewicza 30, PL-30-059 Kraków, Poland.
E-mail: dumanska@uci.agh.edu.pl*
[2]*Institute of Geological Sciences, Polish Academy of Sciences, Research Centre in Kraków, Senacka St. 1,
PL-31002 Kraków, Poland.*
[3]*Polish Geological Institute-National Research Institute, 4 Rakowiecka St., PL-00-975 Warsaw, Poland.*

ABSTRACT:

Dumańska-Słowik, M., Budzyń, B., Heflik, W. and Sikorska, M. 2012. Stability relationships of REE-bearing phosphates in an alkali-rich system (nepheline syenite from the Mariupol Massif, SE Ukraine). *Acta Geologica Polonica*, **62** (2), 247–265.

Primary REE-enriched fluorapatite and fluorbritholite-(Ce) in nepheline syenite from the Mariupol Massif (SE Ukraine), contain textural and chemical evidence of late- to post-magmatic metasomatic alteration. REE mobilization and replacement of the primary phases by fluid-mediated coupled dissolution-reprecipitation strongly depended on the distance between the altered minerals in the host rock. Fluorapatite and fluorbritholite-(Ce) forming individual pristine grains were partially replaced by the same phase with a new composition, resulting in the presence of patchy zoning in altered grains. The increased REE contents in altered fluorapatite rim domains are related to REE mobilization from the altered REE-depleted rim domains of the fluorbritholite-(Ce). The REEs were transported by a fluid with high F activity. The alteration of fluorapatite and fluorbritholite-(Ce) grains in contact resulted in the partial replacement of the primary phases by the same phase with a new composition, but also in the partial replacement of the fluorapatite by secondary monazite and fluorite. The REE mobilized from the fluorbritholite-(Ce) in the presence of a F-rich fluid in an alkali-rich system promoted formation of monazite as the new phosphate REE-host. The presence of secondary parisite in the altered domains of the fluorapatite and fluorbritholite-(Ce) indicates a CO_2 component in the fluid during metasomatic alteration.

Key words: Fluorapatite; Fluorbritholite; Monazite; Rare earth elements; Dissolution-reprecipitation; Mariupolite; Ukraine.

INTRODUCTION

The geochemical behaviour and stability relationships of rare earth elements (REE) -bearing phosphates have been a topic of broad interest for several

decades. Apatite $[Ca_5(PO_4)_3(F,Cl,OH)]$ and monazite $[(REE,Th,U)PO_4]$ are two of the most common phosphate minerals, occurring in almost all varieties of igneous, metamorphic and sedimentary rocks, and two of the main hosts of REEs in the Earth's crust. The sig-

nificant tolerance to structural distortion and chemical composition of apatite-group minerals contribute to the numerous geological, environmental/palaeoenvironmental and technological applications that require an understanding of the substitution mechanisms and other factors controlling the composition of apatites (cf. Pan and Fleet 2002). In general, the REE contents in apatite are low; however, extremely high concentrations of REE_2O_3 (up to ca. 18 wt.%) in apatite were documented in nepheline syenite from the Ilímaussaq alkaline complex, South Greenland (Rønsbo 1989, 2008). Hence, REEs in alkaline rocks do not necessarily concentrate only in monazite as the major phosphate REE-host, giving us the potential to study REE partitioning.

Previous work on the stability relationships of apatite and monazite focused mainly on processes in silica-saturated crystalline rocks (e.g. Bingen *et al.* 1996; Broska and Siman 1998; Finger *et al.* 1998; Wing *et al.* 2003; Broska *et al.* 2005; Janots *et al.* 2006, 2008, 2011; Finger and Krenn 2007; Krenn and Finger 2007; Tomkins and Pattison 2007; Berger *et al.* 2008; Budzyń *et al.* 2010; Ondrejka *et al.* 2012). The textures most typically preserving the constituents of the reaction between REE phosphates and silicates are related to monazite breakdown and the subsequent formation of secondary fluorapatite–allanite–epidote coronas (e.g. Broska and Siman 1998; Finger *et al.* 1998). Since monazite and allanite stability relationhips are strictly dependent on fluid and bulk rock compositions (e.g. Lee and Dodge 1964; Lee and Bastron 1967; Spear 2010; Budzyń *et al.* 2011), the occurrence of allanite is unexpected in low-Ca and high-Na rocks such as syenites. Rather, fluorapatite, britholite and, potentially, monazite may be formed as the main hosts of REEs (cf. Rønsbo 1989, 2008; Budzyń *et al.* 2011). REE mobilization between these phases can be related to primary crystallization from the protolith or to late- to post-magmatic processes. The last two decades have brought significant interest in the metasomatic alteration of the REE-bearing phosphates, particularly in pseudomorphic partial replacements driven by fluid-mediated coupled dissolution-reprecipitation, documented in nature (e.g. Harlov *et al.* 2003, 2007; Hetherington and Harlov 2008; Williams *et al.* 2011; Upadhyay and Pruseth 2012) and reproduced experimentally (e.g. Teufel and Heinrich 1997; Seydoux-Guillaume *et al.* 2002; Harlov and Förster 2003; Harlov *et al.* 2005, 2011; Hetherington *et al.* 2010; Budzyń *et al.* 2011; Williams *et al.* 2011; Harlov and Wirth 2012).

This study documents the stability relationships of REE-enriched fluorapatite, fluorbritholite-(Ce) and monazite in mariupolite, a leucocratic variety of nepheline syenite from the Mariupol alkaline massif (NW part of the eastern Priazovian region, Ukraine). The primary magmatic accessory phases, i.e. fluorapatite and fluorbritholite-(Ce), show evidence of low temperature alteration resulting from fluid-aided coupled dissolution-reprecipitation. Recognition of these processes is crucial in understanding mineral-fluid interactions, stability relationships and REE-partitioning between phosphates.

GEOLOGICAL BACKGROUND AND SAMPLE DESCRIPTION

The Mariupol (Oktyabrski) alkaline massif (Ukrainian Shield, south-eastern Ukraine), which covers an area of ca. 34 km² (e.g. Krivdik *et al.* 2007), is a unique province of Proterozoic alkaline magmatism, with an age constrained to ca. 1.8 Ga (Volkova 2000, 2001). The massif is formed mostly of alkaline syenites and foyaites, with minor amounts of aegirine–albite nepheline syenites (the so-called mariupolite; Morozewicz 1902, 1929), subalkaline gabbros, and their derivatives (peridotites, pyroxenites). Aegirine foyaites and agpaitic phonolites occur mainly among host granitoides in the outer parts of the massif (Text-fig. 1). The vast majority of rocks belong to an agpaitic suite (i.e. containg complex silicates enriched in zirconium, titanium, the rare earth elements, and fluorine) whilst mariupolite is an intermediate variety between miaskitic and agpaitic types (Sharygin *et al.* 2009). Mariupolite covers only a small area (ca. 5-10%) of the whole massif. Further details on the massif can be found in Tichonienkova *et al.* (1967), Donskoy (1982), Solodov (1985), Volkova (2000; 2001) and Krivdik *et al.* (2007).

The leucocratic, fine- to medium-grained variety of nepheline syenite (mariupolite) shows porphyritic and chaotic or, locally, fluidal textures. The main mineral assemblage includes albite ($Ab_{94-92}An_{6-8}$), nepheline and aegirine with subordinate amounts of lepidomelane, K-feldspar, pyrochlore, sodalite, natrolite, zircon, fluorite, cancrinite, fluorapatite, fluorbritholite and monazite. The predominant mineral is albite, forming fine prismatic grains with rare twinning, or large grains of an older generation defining the porphyritic fabric of the rock. The nepheline forms large, dynamically deformed crystals with patchy extinction. The lepidomelane and cancrinite grains concentrate mainly close to the sodalite and natrolite aggregates. The K-feldspar forms large tabular grains, which occasionally reveal a crosshatched microcline pattern. Zircon crys-
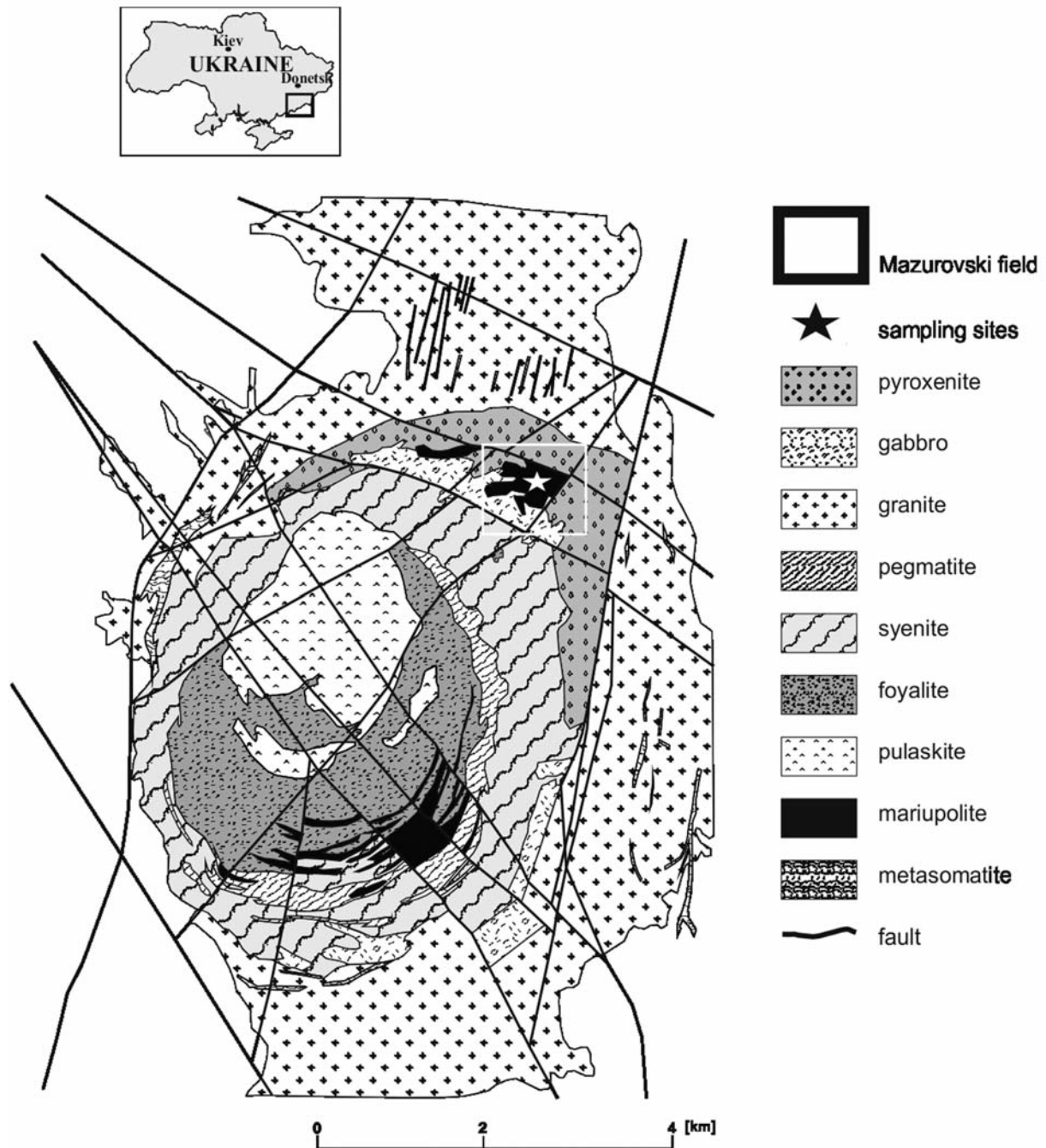
Text-fig. 1. A geological map of the Mariupol massif (SE Ukraine) (modified from Dumańska-Słowik *et al.* 2011b)

tallizes as euhedral grains with oscillatory zoning along the rims and irregular patchy zoning in the cores (Dumańska-Słowik *et al.* 2011a). Euhedral to subhedral grains of pyrochlore are present in the interstices between the albite grains. The pyrochlore is surrounded by coronas of acicular Fe-chlorite. A more detailed mineralogical description of the mariupolite is presented by Dumańska-Słowik *et al*. (2011b).

ANALYTICAL PROCEDURES

Preliminary observations were performed on polished thin sections using a FEI Quanta 200 field emission gun scanning electron microscope (SEM) equipped with an EDAX energy dispersive spectrometer (EDS) at the Department of Mineralogy, Petrography and Geochemistry, the AGH University of Science and Techno-

MAGDALENA DUMAŃSKA-SŁOWIK *ET AL.*

fluorapatite					fluorbritholite					monazite				
acceleration voltage 15 kV, beam current 10 or 20 nA					acceleration voltage 15 kV, beam current 10 or 20 nA					acceleration voltage 20 kV, beam current 50 nA				
element	signal	WDS crystal	standard	estimated detection limit (ppm)	element	signal	WDS crystal	standard	estimated detection limit (ppm)	element	signal	WDS crystal	standard	estimated detection limit (ppm)
Pr	Lβ	LIF	PrP_5O_{14}	2904	Ca	Kα	PET	wollastonite	285	P	Kα	PET	apatite	181
Nd	Lβ	LIF	NdP_5O_{14}	2993	La	Lα	PET	LaB_6	1124	La	Lα	LIF	LaB_6	652
Mn	Kα	LIF	rhodonite	879	Ce	Lα	PET	CeP_5O_{14}	1129	Ce	Lα	LIF	CeP_5O_{14}	466
Sm	Lβ	LIF	SmP_5O_{14}	2802	P	Kα	PET	apatite BB_3	350	Pr	Lβ	LIF	PrP_5O_{14}	855
Fe	Kα	LIF	Fe_2O_3	777	Th	Mα	PET	ThO_2 synt	2103	Nd	Lβ	LIF	NdP_5O_{14}	788
Gd	Lβ	LIF	GdP_5O_{14}	2751	U	Mβ	LIF	vorlanite	1671	Sm	Lβ	LIF	SmP_5O_{14}	1729
Er	Lα	LIF	REE1	3937	Cl	Kα	PET	tugtupite	327	Gd	Lβ	LIF	GdP_5O_{14}	1508
Dy	Lβ	LIF	REE1	7211	S	Kα	PET	barite	186	Tb	Lβ	LIF	TbP_5O_{14}	1550
Yb	Lα	LIF	REE3	3100	Pr	Lβ	LIF	PrP_5O_{14}	2904	Dy	Lβ	LIF	DyP_5O_{14}	1606
Ho	Lβ	LIF	REE2	7310	Fe	Kα	LIF	Fe_2O_3	777	Ho	Lβ	LIF	HoP_5O_{14}	1641
F	Kα	TAP	phlogopite	2908	Mn	Kα	LIF	rhodonite	879	Er	Lα	LIF	ErP_5O_{14}	839
Na	Kα	TAP	albite	322	Nd	Lβ	LIF	NdP_5O_{14}	2993	Yb	Lα	LIF	YbP_5O_{14}	914
Sr	Lα	TAP	$SrTiO_3$	522	Sm	Lβ	LIF	SmP_5O_{14}	2802	Pb	Mβ	PET	$PbCrO_4$	397
Si	Kα	TAP	wollastonite	216	Gd	Lβ	LIF	GdP_5O_{14}	2751	U	Mβ	PET	vorlanite	177
Y	Lα	TAP	YAG	615	Er	Lα	LIF	REE1	3937	Th	Mα	PET	ThO_2 synt	525
P	Kα	PET	apatite BB_3	350	Dy	Lβ	LIF	REE1	7211	Ca	Kα	PET	wollastonite	64
Ca	Kα	PET	wollastonite	285	Yb	Lα	LIF	REE3	3100	S	Kα	PET	barite	97
Cl	Kα	PET	tugtupite	328	Ho	Lβ	LIF	REE2	7310	Y	Lα	TAP	YAG	221
La	Lα	PET	LaB_6	977	F	Kα	TAP	phlogopite	2344	Si	Kα	TAP	wollastonite	76
Ce	Lα	PET	CeP_5O_{14}	970	Na	Kα	TAP	albite	188					
As	Lα	TAP	GaAs	500	As	Lα	TAP	GaAs	436					
S	Kα	PET	barite	180	Si	Kα	TAP	wollastonite	216					
					Sr	Lα	TAP	$SrTiO_3$	615					
					Y	Lα	TAP	YAG	487					

Table 1. Electron microprobe analyses conditions for REE minerals

logy, Kraków; and a LEO 1430 SEM equipped with an Oxford ISIS 300 system at the Polish Geological National Research Institute in Warsaw. Chemical analyses were conducted using a Cameca SX-100 electron microprobe at the Inter-Institute Analytical Complex for Minerals and Synthetic Substances at Warsaw University. Electron microprobe operating conditions, standards and detection limits are presented in Table 1. The raw data were corrected using the PAP procedure (Pouchou and Pichoir 1985).

Analyte Symbol	SiO_2	Al_2O_3	Fe_2O_3	MnO	MgO	CaO	Na_2O	K_2O	TiO_2	P_2O_5	As	Sc	Cr	LOI	Total
Unit Symbol	%	%	%	%	%	%	%	%	%	%	ppm	ppm	ppm	%	%
Detection Limit	0.01	0.01	0.01	0.001	0.01	0.01	0.01	0.01	0.001	0.01	0.5	0.1	5	0.01	0.01
Mariupolite	60.16	20.61	3.55	0.06	0.06	0.37	12.11	1.63	0.05	< 0.01	2.50	2.60	< 5	0.46	99.07

Analyte Symbol	Th	U	Y	La	Ce	Pr	Nd	Sm	Eu	Gd	Tb	Dy	Ho	Er	Tm	Yb	Lu
Unit Symbol	ppm	ppm	ppm	ppm	ppm	ppm	ppm	ppm	ppm	ppm	ppm	ppm	ppm	ppm	ppm	ppm	ppm
Detection Limit	0.1	0.1	2	0.1	0.1	0.05	0.1	0.1	0.05	0.1	0.1	0.1	0.1	0.1	0.05	0.1	0.04
Mariupolite	20.1	9.2	13	41.8	117	13.5	46.9	7.2	0.72	4	0.6	3.6	0.7	2.3	0.43	3.6	0.81

Analyte Symbol	Sc	Be	V	Cr	Co	Ni	Cu	Zn	Ga	Ge	As	Rb	Sr	Zr	Nb	Mo
Unit Symbol	ppm	ppm	ppm	ppm	ppm	ppm	ppm	ppm	ppm	ppm	ppm	ppm	ppm	ppm	ppm	ppm
Detection Limit	1	1	5	20	1	20	10	30	1	1	5	2	2	4	1	2
Mariupolite	2	3	26	< 20	5	< 20	< 10	40	80	3	< 5	111	35	1812	620	< 2

Analyte Symbol	In	Sn	Sb	Cs	Ba	Hf	Ta	W	Tl	Pb	Bi	Cu	Ni	Zn	S	Ag	Pb
Unit Symbol	ppm	ppm	ppm	ppm	ppm	ppm	ppm	ppm	ppm	ppm	ppm	ppm	ppm	ppm	%	ppm	ppm
Detection Limit	0.2	1	0.5	0.5	3	0.2	0.1	1	0.1	5	0.4	1	1	1	0.001	0.3	5
Mariupolite		30	< 0.5	< 0.5	8	44.4	34.1	25	0.4	12	< 0.4	4	4	44	0.002	0.5	< 5

Table 2. Bulk rock composition of the mariupolite

Bulk-rock analyses were performed in the Actlabs Activation Laboratories Ltd., Ancaster, Ontario, Canada. The abundances of major oxides and trace elements were determined using Inductively Coupled Plasma-Optical Emission Spectrometry (ICP-OES) and Inductively Coupled Plasma-Mass Spectrometry (ICP-MS), following lithium metaborate/tetraborate fusion and dilute nitric digestion. Major oxides and trace elements were analysed using Thermo Jarrell-Ash EN-VIRO II ICP or a Spectro Cirros ICP and Perkin Elmer SCIEX ELAN 6000 ICP-MS, respectively. Calibration was performed using multiple USGS and CAN-MET certified reference materials. The results of the whole rock analysis are presented in Table 2.

RESULTS

The phosphate mineral assemblage in the mariupolite comprises mainly fluorbritholite-(Ce) and fluorapatite, whilst monazite occurs in minor amounts. Both fluorbritholite-(Ce) and fluorapatite occur as individual matrix grains.

The fluorapatite forms anhedral, individual grains (up to 3 mm in size) dispersed in the mariupolite matrix near lepidomelane, feldspar, zircon and nepheline. It shows patchy zoning (c. 2) with dark domains in high contrast BSE imaging, which dominate in the inner parts of grains, while the bright domains are present along rims, and penetrate the grain interiors leaving the dark domains that seem to look like subgrains (Text-fig. 2). The bright domains along the rims show sharp boundaries with the internal zones, and occasionally contain inclusions of parisite (Text-fig. 2c). The fluorapatite is significantly enriched in REEs, and reflects some compositional variation between the domains. The bright domains contain 13.6–16.6 wt.% REE_2O_3 versus 10.5–12.5 wt.% in dark domains (Table 3). The Na content is also elevated, and differs between the bright and dark domains, i.e. from 2.2–2.6 wt.% to 1.6–1.8 wt.% Na_2O, respectively (Table 3). The enrichment in Na and REEs is accompanied by a decrease in the Ca content (Text-fig. 3). The concentrations of Si, Sr and Mn are similar within the fluorapatite, and do not reflect variations between the internal domains.

The fluorbritholite-(Ce) usually occurs in association with albite, aegirine, zircon and pyrochlore. It forms individual anhedral matrix grains up to 700 μm that exhibit patchy zoning in high contrast BSE imaging (Text-fig. 4). The boundaries between the bright and dark domains display irregular shapes. In general, the bright domains are present in the inner parts, while

the rims are dominated by the dark domains. The grain boundaries show irregular, lobate shapes suggesting that the grains are corroded. Single inclusions of fluorapatite and natrolite concentrating mainly near the rims of the grain are found rarely. The fluorbritholite shows some variation in composition between bright and dark domains. The bright domains are enriched in REE (56.3–60.1 wt.% REE_2O_3) compared to the dark domains (53.4-55.2 wt.% REE_2O_3; Table 4). Simi-
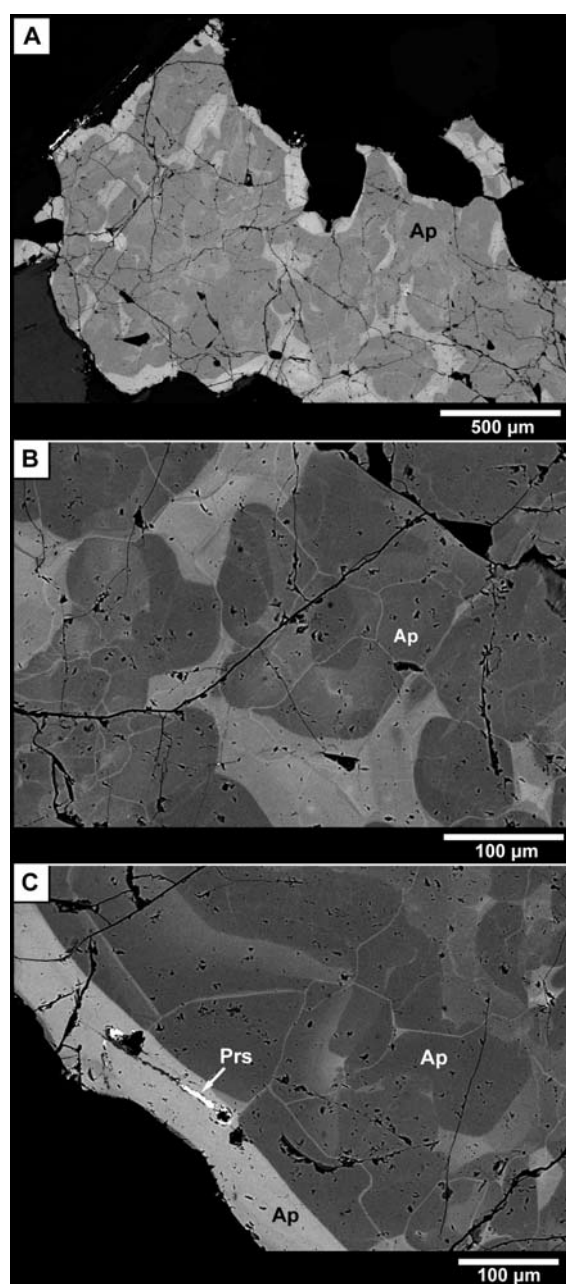
Text-fig. 2. The patchy zoned fluorapatite (Ap) grain in high contrast BSE imaging. Dark domains dominate in the core. Secondary parisite (Prs) inclusions occasionally are present in the bright compositional domains along rims

larly, the bright domains are distinctly depleted in Ca and Th (13.3–15.1 wt.% CaO; 0.4–0.6 wt.% ThO_2) in opposite to the dark patches domains (15.8–17.2 wt.% CaO; 0.7–1.5 wt.% ThO_2). Hence, the distinct enrich-ment in REEs is accompanied by significant decrease of Ca+Th content. Negative correlations of 2(REE) vs Ca+Th ($r = -0.979$) and Si+REE vs Ca+P ($r = -0.991$) are observed in fluorbritholite-(Ce).
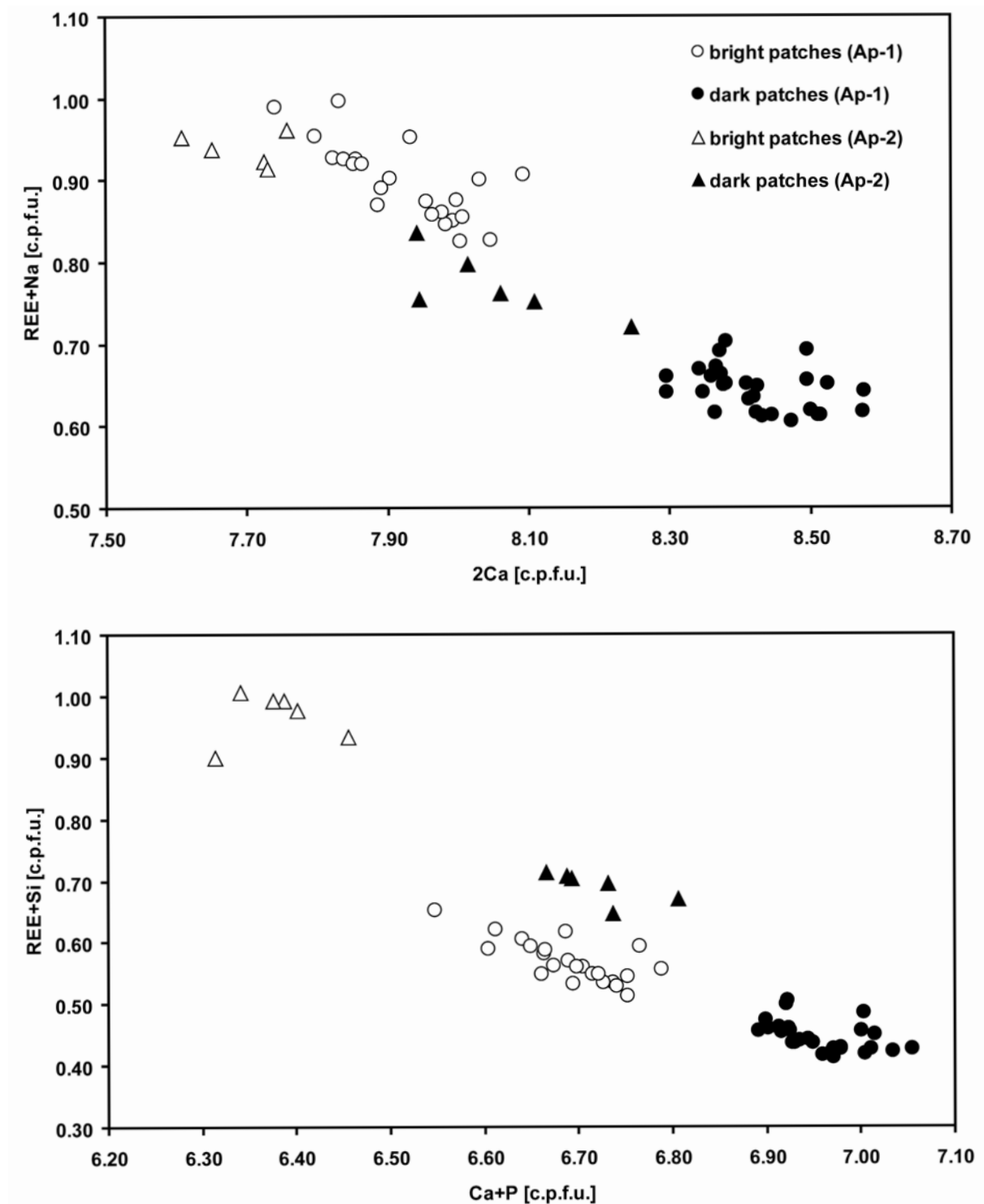
Text-fig. 3. Plots of formula proportions 2Ca vs. (REE + Na) and (Ca + P) vs. (REE + Si) calculated on the basis of 13 O atoms for the fluorapatite in the mariupolite.

Ap-1 – the fluorapatite present as individual grains; Ap-2 – the fluorapatite in contact with the fluorbritholite

STABILITY RELATIONSHIPS OF REE-BEARING PHOSPHATES IN AN ALKALI-RICH SYSTEM

Fluorbritholite-(Ce) grains occasionally are closely associated with fluorapatite in the matrix. The grain boundaries between fluorbritholite-(Ce) and fluorapatite are filled with a fine-grained symplectite of monazite and fluorite grains, which are also present as inclusions within the fluorapatite (Text-fig. 5). The symplectitic monazite forms anhedral grains up to ca. 100 μm in size. The monazite also forms elongated, up to ca. 200 μm, grains that partially surround the fluorapatite.

The fluorbritholite-(Ce) associated with fluorapatite shows patchy zoning in high contrast BSE imaging, with dark domains in the core and bright domains along the rims that occasionally contain small inclusions of arasite [$Ca(Ce,La)_2(CO_3)_3F$]. The bright and dark domains contain similar concentrations of REEs (58.3–60.2 wt.% vs. 58.6–58.9 wt.% REE_2O_3, respectively), Th (0.9–1.1 wt.% vs. 0.8–1.0 wt.% ThO_2, respectively) and P (2.2–3.4 wt.% vs. 1.8–2.7 wt.% P_2O_5, respectively). The differences are found

| Region of crystal | Individual pristine grain of fluorapatite | | | | | | | | | | | |
| | Bright domains | | | | | | | | | | | |
Analysis	1	10	15	18	24	25	26	31	34	35	105	110
P_2O_5	36.29	36.02	35.87	34.29	35.80	36.32	36.91	36.50	36.16	36.37	36.23	35.50
SiO_2	0.79	0.93	1.00	1.09	0.93	0.91	0.79	0.74	0.77	0.85	0.76	1.11
Y_2O_3	0.46	0.50	0.39	0.43	0.43	0.41	0.35	0.44	0.42	0.35	0.41	0.42
La_2O_3	2.77	2.74	2.76	2.98	2.68	2.69	2.53	2.51	2.69	2.53	2.93	3.08
Ce_2O_3	6.58	6.97	6.99	7.41	6.59	6.75	6.47	6.13	6.60	6.61	7.10	7.31
Pr_2O_3	0.93	0.79	0.90	1.03	0.93	1.03	0.81	0.96	0.46	0.79	0.56	0.78
Nd_2O_3	3.67	3.62	3.24	3.85	3.43	3.49	3.28	3.14	3.44	3.23	3.74	3.88
Sm_2O_3	0.68	0.36	0.41	0.40		0.51	0.74		0.60	0.53		
Gd_2O_3	0.41	0.52	0.45	0.52			0.44	0.40		0.46		
CaO	40.76	41.09	41.29	40.31	41.77	41.28	42.18	41.97	41.84	41.79	42.25	40.91
MnO	0.26	0.22	0.24	0.31	0.23	0.26	0.23	0.42	0.39	0.28	0.24	0.22
SrO	0.37	0.33	0.31	0.29	0.32	0.33	0.36	0.37	0.36	0.43	0.29	0.26
Na_2O	2.40	2.41	2.34	2.52	2.25	2.32	2.18	2.20	2.38	2.23	2.43	2.49
F	3.72	3.89	3.91	4.24	3.98	3.77	3.71	3.84	4.08	3.82	3.43	3.53
H_2O											0.06	0.00
sum	100.09	100.39	100.10	99.67	99.34	100.07	100.98	99.62	100.19	100.27	100.44	99.48
-O=F	1.57	1.64	1.65	1.79	1.68	1.59	1.56	1.62	1.72	1.61	1.44	1.49
total	98.52	98.75	98.45	97.88	97.66	98.48	99.42	98.00	98.47	98.66	99.00	98.00
REE_2O_3	15.50	15.50	15.14	16.62	14.06	14.88	14.62	13.58	14.21	14.50	14.75	15.47
Cations per formula unit on the basis of 13 oxygens												
P	2.752	2.721	2.713	2.632	2.711	2.743	2.760	2.750	2.716	2.739	2.742	2.720
Si	0.071	0.083	0.089	0.099	0.083	0.081	0.070	0.066	0.068	0.076	0.068	0.100
Y	0.022	0.024	0.019	0.021	0.020	0.019	0.016	0.021	0.020	0.017	0.020	0.020
La	0.092	0.090	0.091	0.100	0.088	0.089	0.082	0.082	0.088	0.083	0.097	0.103
Ce	0.216	0.228	0.229	0.246	0.216	0.220	0.209	0.200	0.214	0.215	0.232	0.242
Pr	0.030	0.026	0.029	0.034	0.030	0.033	0.026	0.031	0.015	0.026	0.018	0.026
Nd	0.117	0.115	0.103	0.125	0.110	0.111	0.103	0.100	0.109	0.103	0.119	0.125
Sm	0.021	0.011	0.013	0.012		0.016	0.023		0.018	0.016		
Gd	0.012	0.015	0.013	0.016			0.013	0.012		0.014		
Ca	3.912	3.928	3.952	3.916	4.003	3.946	3.992	4.002	3.978	3.982	4.047	3.966
Mn	0.020	0.017	0.018	0.024	0.017	0.020	0.017	0.032	0.029	0.021	0.018	0.017
Sr	0.019	0.017	0.016	0.015	0.017	0.017	0.018	0.019	0.019	0.022	0.015	0.014
Na	0.417	0.417	0.405	0.443	0.390	0.401	0.373	0.380	0.409	0.385	0.420	0.436
F	1.054	1.098	1.105	1.216	1.126	1.064	1.036	1.081	1.145	1.075	0.970	1.010
OH											0.036	0.000
Total cations	7.701	7.692	7.691	7.682	7.687	7.697	7.704	7.695	7.684	7.698	7.797	7.770
REE	0.510	0.509	0.497	0.553	0.465	0.489	0.473	0.446	0.465	0.473	0.486	0.516

Notes: Blank = below EMP detection limit. All analyses of As, Dy, Ho, Er, Yb, Th, U, S and Cl are below detection limit and therefore not included in the table.

Table 3A. Representative electron microprobe analyses of the fluorapatite

MAGDALENA DUMAŃSKA-SŁOWIK *ET AL.*

| Region of crystal | Individual pristine grain of fluorapatite | | | | | | | | | | | | | |
| | Dark domains | | | | | | | | | | | | | |
Analysis	2	4	5	11	12	13	33	38	104	106	107	108	109	111
P_2O_5	37.47	38.01	37.54	37.73	37.00	37.14	36.63	37.68	37.45	37.51	36.73	37.33	37.06	37.04
SiO_2	0.92	0.89	0.96	0.98	1.07	0.92	1.05	0.92	0.96	0.80	1.15	0.93	1.12	1.18
Y_2O_3	0.23	0.31	0.27	0.26	0.33	0.29	0.31	0.36	0.31	0.30	0.31	0.27	0.30	0.30
La_2O_3	1.85	1.84	1.99	2.07	2.11	1.95	2.07	2.03	1.98	2.04	2.28	1.99	2.36	2.39
Ce_2O_3	5.02	5.08	4.86	5.19	5.34	5.03	5.23	4.85	5.15	5.15	5.93	5.15	5.49	5.80
Pr_2O_3	0.68	0.69	0.68	0.59	0.64	0.78	0.73	0.84	0.74	0.63	0.81	0.67	0.73	0.60
Nd_2O_3	2.60	2.37	2.62	2.63	2.63	2.53	2.59	2.38	2.39	2.50	3.13	2.85	3.06	3.20
Sm_2O_3	0.49	0.39	0.39	0.41	0.41	0.49	0.51	0.48				0.61		
Gd_2O_3										0.50				
CaO	45.32	45.24	45.84	45.06	44.94	45.11	44.97	45.61	46.17	45.94	44.51	45.68	45.12	44.80
MnO	0.25	0.32	0.13	0.23	0.28	0.16	0.17	0.16	0.22	0.18	0.22	0.27	0.19	0.29
SrO	0.31	0.38	0.32	0.33	0.33	0.31	0.30	0.32	0.29	0.23	0.22	0.30	0.28	0.26
Na_2O	1.57	1.65	1.57	1.71	1.67	1.66	1.65	1.57	1.66	1.70	1.76	1.67	1.79	1.75
F	3.83	3.78	3.93	3.82	3.94	3.93	4.00	3.82	3.65	3.29	3.53	3.35	2.89	3.58
H_2O									0.00	0.16	0.05	0.14	0.35	0.03
sum	100.54	100.95	101.10	101.01	100.69	100.30	100.21	101.02	100.95	100.91	100.62	101.22	100.74	101.21
-O=F	1.61	1.59	1.65	1.61	1.66	1.65	1.68	1.61	1.54	1.39	1.49	1.41	1.21	1.51
total	98.93	99.36	99.45	99.40	99.03	98.65	98.53	99.41	99.42	99.52	99.14	99.80	99.52	99.71
REE_2O_3	10.9	10.7	10.8	11.2	11.5	11.1	11.4	10.9	10.56	11.11	12.46	11.54	11.93	12.29
Cations per formula unit on the basis of 13 oxygens														
P	2.755	2.777	2.742	2.762	2.725	2.739	2.711	2.757	2.748	2.767	2.733	2.753	2.756	2.735
Si	0.080	0.077	0.083	0.085	0.093	0.080	0.092	0.080	0.083	0.070	0.101	0.081	0.098	0.103
Y	0.011	0.014	0.012	0.012	0.015	0.013	0.014	0.017	0.014	0.014	0.014	0.013	0.014	0.014
La	0.059	0.059	0.063	0.066	0.068	0.063	0.067	0.065	0.063	0.065	0.074	0.064	0.076	0.077
Ce	0.160	0.160	0.153	0.164	0.170	0.160	0.167	0.153	0.163	0.164	0.191	0.164	0.177	0.185
Pr	0.022	0.022	0.021	0.019	0.020	0.025	0.023	0.026	0.023	0.020	0.026	0.021	0.023	0.019
Nd	0.081	0.073	0.081	0.081	0.082	0.079	0.081	0.073	0.074	0.078	0.098	0.089	0.096	0.100
Sm	0.015	0.012	0.012	0.012	0.012	0.015	0.015	0.014				0.018		
Gd										0.014				
Ca	4.216	4.183	4.237	4.174	4.188	4.210	4.212	4.223	4.287	4.289	4.190	4.263	4.247	4.186
Mn	0.018	0.023	0.009	0.017	0.021	0.012	0.013	0.012	0.016	0.013	0.017	0.020	0.014	0.021
Sr	0.016	0.019	0.016	0.017	0.017	0.016	0.015	0.016	0.015	0.012	0.011	0.015	0.014	0.013
Na	0.264	0.276	0.263	0.287	0.282	0.280	0.280	0.263	0.278	0.287	0.299	0.281	0.306	0.297
F	1.052	1.032	1.072	1.045	1.084	1.083	1.106	1.044	1.000	0.907	0.980	0.924	0.802	0.988
OH									0.000	0.093	0.029	0.081	0.205	0.017
Total cations	7.695	7.694	7.692	7.694	7.693	7.692	7.691	7.699	7.765	7.792	7.753	7.782	7.822	7.749
REE	0.346	0.340	0.343	0.354	0.367	0.355	0.368	0.349	0.338	0.355	0.403	0.369	0.386	0.395

Notes: Blank = below EMP detection limit. All analyses of As, Dy, Ho, Er, Yb, Th, U, S and Cl are below detection limit and therefore not included in the table.

Table 3B. Representative electron microprobe analyses of the fluorapatite

in the concentrations of Ca and Si. Lower contents of 8.0–9.5 wt.% CaO and 18.0–18.5 SiO_2 are found in the bright domains, and higher content of 9.9–11.3 wt.% CaO and 18.6–19.7 wt.% SiO_2 in the dark domains.

The compositions of the dark and bright domains in the fluorapatite associated with fluorbritholite-(Ce) vary strongly. These variations include 2.2–2.5 wt.% SiO_2 in dark domains vs. 2.4–4.0 wt.% SiO_2 in bright domains, 34.5–35.8 wt.% P_2O_5 in dark domains vs.

31.2–33.0 wt.% P_2O_5 in bright domains, and 13.2–15.1 wt.% REE_2O_3 in dark domains vs. 17.1–19.1 wt.% REE_2O_3 in bright domains. Compared to individual grains of fluorapatite, the fluorapatite associated with fluorbritholite-(Ce) has higher contents of Si, Sr, Y and LREE, and lower contents of Ca, F and HREE (Text-fig. 6).

The monazite composition is typical of monazite-(Ce), although there are variable La and Nd contents (0.38 to 0.93 Nd/La; Table 5). The monazite

| Region of crystal | Fluorapatite associated with fluorbritholite | | | | | | | | | | | |
| | Bright domains | | | | | | Dark domains | | | | | |
Analysis	101	103	107	108	110	112	102	104	105	106	109	111
P_2O_5	31.21	31.82	31.69	32.78	31.60	32.99	34.86	35.75	34.67	34.82	34.51	35.30
SiO_2	3.81	3.83	3.82	3.38	3.99	2.44	2.27	2.51	2.16	2.36	2.31	2.19
Y_2O_3	1.19	0.87	0.96	0.67	1.28	0.83	0.57	0.71	0.52	0.56	0.57	0.85
La_2O_3	3.17	3.23	3.43	3.39	3.27	3.99	2.69	2.82	2.89	2.88	2.93	2.31
Ce_2O_3	7.84	8.68	8.43	8.61	7.68	8.80	6.47	7.03	7.31	6.83	6.94	6.09
Pr_2O_3	1.09	1.28	0.86	1.00	1.25	1.35	0.88	0.81	0.53	0.49		
Nd_2O_3	3.81	4.07	4.04	4.18	4.11	4.09	3.07	3.01	3.85	3.48	3.98	3.92
Sm_2O_3												
Gd_2O_3												
CaO	37.91	38.46	37.57	38.63	37.45	36.29	42.32	41.33	40.36	41.65	40.69	41.52
MnO	0.45	0.31	0.37	0.27	0.40	0.26	0.22	0.25	0.28	0.19	0.23	0.39
SrO	0.54	0.45	0.55	0.45	0.40	0.37	0.45	0.45	0.37	0.41	0.50	0.47
Na_2O	1.88	1.60	1.67	1.64	1.76	2.47	1.46	1.57	1.81	1.55	1.72	1.79
F	2.80	3.10	2.74	2.72	2.90	3.33	2.72	2.71	2.88	2.97	2.87	2.95
H_2O	0.25	0.14	0.28	0.32	0.21	0.00	0.36	0.40	0.27	0.25	0.28	0.26
sum	95.93	97.82	96.41	98.04	96.30	97.19	98.35	99.34	97.91	98.44	97.53	98.03
-O=F	1.18	1.30	1.16	1.14	1.22	1.40	1.15	1.14	1.21	1.25	1.21	1.24
total	94.75	96.52	95.25	96.89	95.08	95.79	97.20	98.20	96.70	97.19	96.32	96.79
REE_2O_3	17.09	18.13	17.71	17.84	17.58	19.05	13.68	14.38	15.11	14.24	14.41	13.17
	Cations per formula unit on the basis of 13 oxygens											
P	2.523	2.525	2.551	2.592	2.537	2.639	2.684	2.715	2.696	2.678	2.686	2.707
Si	0.363	0.359	0.363	0.316	0.379	0.231	0.207	0.225	0.199	0.214	0.213	0.198
Y	0.060	0.044	0.048	0.033	0.064	0.041	0.028	0.034	0.026	0.027	0.028	0.041
La	0.112	0.112	0.120	0.117	0.114	0.139	0.090	0.093	0.098	0.097	0.099	0.077
Ce	0.274	0.298	0.293	0.294	0.267	0.304	0.215	0.231	0.246	0.227	0.233	0.202
Pr	0.038	0.044	0.030	0.034	0.043	0.046	0.029	0.026	0.018	0.016		
Nd	0.130	0.136	0.137	0.139	0.139	0.138	0.100	0.096	0.126	0.113	0.131	0.127
Sm												
Gd												
Ca	3.879	3.863	3.826	3.865	3.804	3.675	4.123	3.973	3.971	4.054	4.007	4.030
Mn	0.036	0.025	0.030	0.021	0.032	0.021	0.017	0.019	0.022	0.015	0.018	0.030
Sr	0.030	0.024	0.030	0.025	0.022	0.020	0.024	0.023	0.020	0.021	0.027	0.025
Na	0.348	0.290	0.308	0.296	0.324	0.453	0.258	0.273	0.322	0.272	0.306	0.314
F	0.846	0.918	0.825	0.803	0.871	0.994	0.783	0.770	0.838	0.854	0.833	0.845
OH	0.159	0.088	0.178	0.199	0.133	0.000	0.218	0.239	0.165	0.151	0.172	0.157
Total cations	7.793	7.720	7.737	7.733	7.727	7.708	7.774	7.709	7.742	7.735	7.747	7.751
REE	0.614	0.633	0.629	0.618	0.628	0.669	0.462	0.481	0.513	0.480	0.491	0.447

Notes: Blank = below EMP detection limit. All analyses of As, Dy, Ho, Er, Yb, Th, U, S and Cl are below detection limit and therefore not included in the table.

Table 3C. Representative electron microprobe analyses of the fluorapatite

has a low ThO_2 content, ranging from 0.5 to 1.6 wt.%. The concentrations of U and Pb are below the detection limit of the electron microprobe. It should be also noted that REEs from Eu to Lu, except three analytical spots with 0.7–1.0 wt.% Gd_2O_3, are also below detection limits. Based on the plot of formula proportions (REE + P) vs. (Th + Si), substitution of the huttonitic component predominates over substitution of the cheralitic component in the monazite (Text-fig. 7).

DISCUSSION

The individual matrix grains of fluorapatite in mariupolite are interpreted as primary accessory phases crystallized during the early magmatic stage. The temperature of crystallization can be roughly constrained at ca. 600°C, with an interval of within 60–100°C based on the estimated apatite saturation temperature equation given in Piccoli and Candela (2002). Fluorapatite with extremely high REE_2O_3

256

MAGDALENA DUMAŃSKA-SŁOWIK *ET AL.*
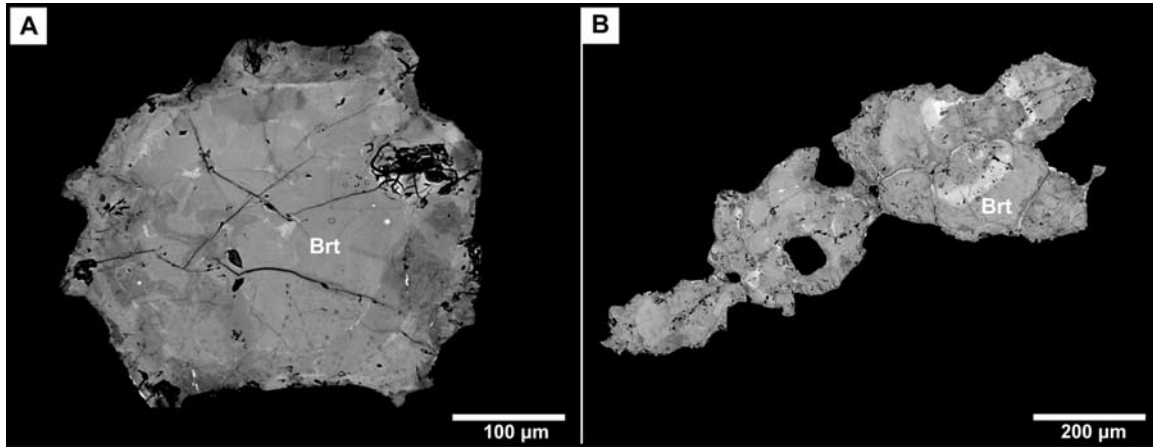
Text-fig. 4. The patchy zoned fluorbritholite-(Ce) (Brt) in high contrast BSE imaging. The internal textures of the grains resulted from the partial alteration of the primary phase via the fluid-aided coupled dissolution-reprecipitation process
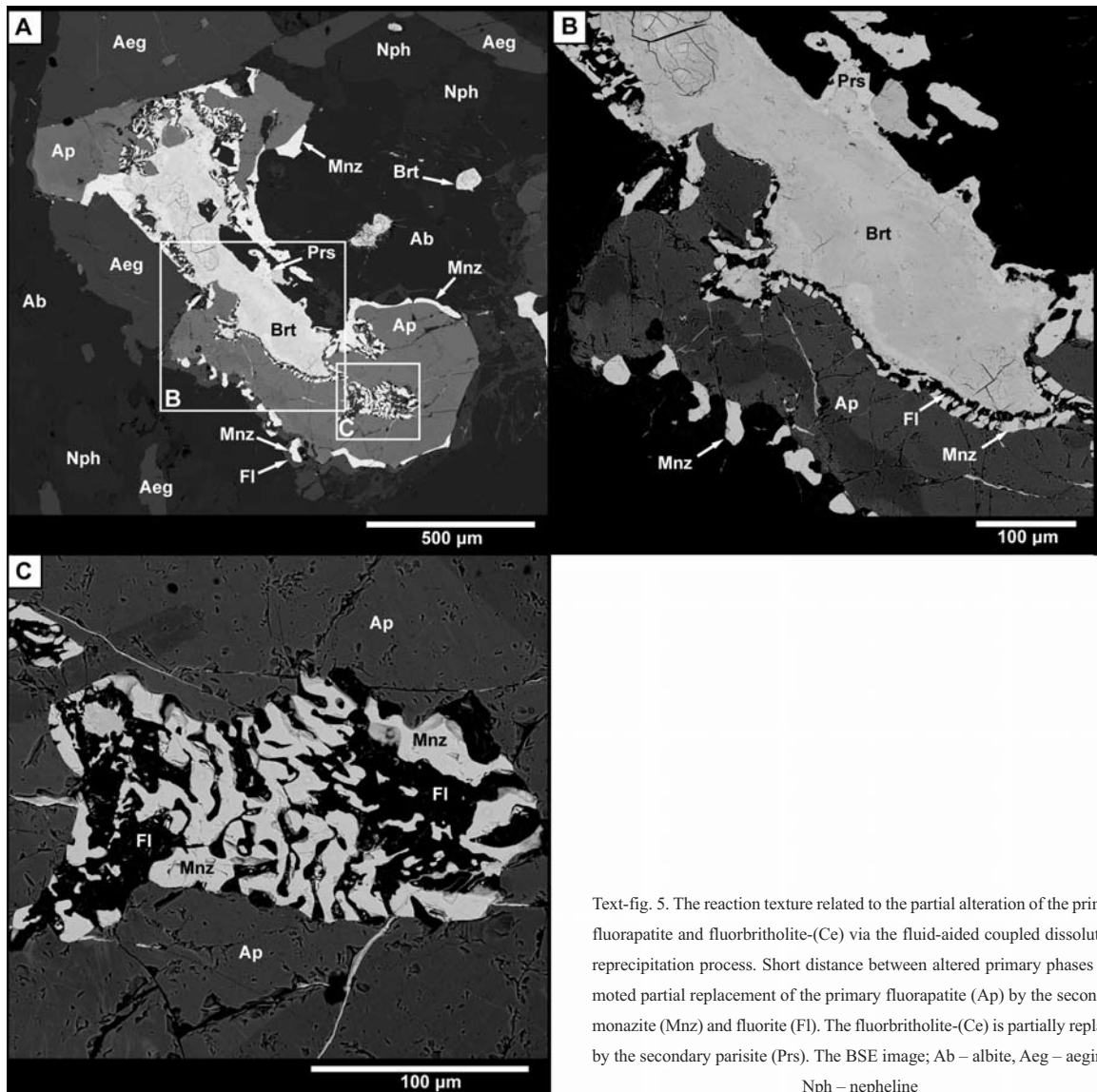
Text-fig. 5. The reaction texture related to the partial alteration of the primary fluorapatite and fluorbritholite-(Ce) via the fluid-aided coupled dissolution-reprecipitation process. Short distance between altered primary phases promoted partial replacement of the primary fluorapatite (Ap) by the secondary monazite (Mnz) and fluorite (Fl). The fluorbritholite-(Ce) is partially replaced by the secondary parisite (Prs). The BSE image; Ab – albite, Aeg – aegirine, Nph – nepheline

STABILITY RELATIONSHIPS OF REE-BEARING PHOSPHATES IN AN ALKALI-RICH SYSTEM

| | Individual pristine grain of fluorbritholite | | | | | | |
	Bright domains						
Analysis	1	6	7	8	14	19	21
P_2O_5	2.25	2.96	3.71	2.23	3.05	3.21	3.47
SiO_2	20.14	19.66	19.19	19.83	19.80	19.38	19.59
ThO_2	0.45	0.55	0.48	0.51	0.54	0.62	0.61
Y_2O_3	1.17	1.23	1.57	1.24	1.47	1.51	1.93
La_2O_3	13.55	12.24	12.89	13.49	12.45	12.99	12.74
Ce_2O_3	29.15	27.86	26.51	28.55	27.97	26.86	26.28
Pr_2O_3	2.57	2.79	2.74	2.74	2.57	2.80	2.67
Nd_2O_3	11.16	11.38	10.02	10.19	10.81	9.87	9.91
Sm_2O_3	1.82	1.16	1.67	1.39	1.45	1.46	1.35
Gd_2O_3	0.73	0.70	0.98	0.88	0.57	0.89	1.38
CaO	13.30	14.72	15.15	13.52	14.76	14.77	15.05
MnO	0.36	0.39	0.38	0.38	0.36	0.36	0.31
SrO							
Na_2O			0.06				
F	1.51	1.39	1.50	1.61	1.22	1.37	1.37
Cl							
H_2O	0.43	0.50	0.45	0.37	0.58	0.50	0.51
Sum	98.60	97.50	97.31	96.92	97.59	96.59	97.16
-O=(F+Cl)	0.64	0.58	0.63	0.68	0.52	0.58	0.58
total	97.96	96.92	96.68	96.24	97.07	96.01	96.59
REE_2O_3	60.15	57.34	56.39	58.47	57.28	56.37	56.26
P	0.250	0.327	0.407	0.251	0.336	0.357	0.380
Si	2.640	2.566	2.482	2.631	2.578	2.541	2.537
Th	0.014	0.016	0.014	0.015	0.016	0.019	0.018
Y	0.082	0.086	0.108	0.087	0.102	0.105	0.133
La	0.655	0.589	0.615	0.660	0.598	0.628	0.608
Ce	1.399	1.331	1.256	1.386	1.333	1.289	1.246
Pr	0.123	0.133	0.129	0.132	0.122	0.134	0.126
Nd	0.523	0.530	0.463	0.483	0.503	0.462	0.458
Sm	0.082	0.052	0.075	0.063	0.065	0.066	0.060
Gd	0.032	0.030	0.042	0.039	0.025	0.039	0.059
Ca	1.869	2.058	2.100	1.922	2.058	2.075	2.089
Mn	0.040	0.043	0.042	0.042	0.040	0.040	0.034
Sr							
Na			0.015				
F	0.627	0.572	0.614	0.676	0.504	0.570	0.560
Cl	0.000	0.000	0.000	0.000	0.000	0.000	0.000
OH	0.376	0.435	0.388	0.327	0.504	0.437	0.441
Total cations	7.708	7.761	7.749	7.713	7.774	7.755	7.749
REE	2.895	2.751	2.688	2.851	2.747	2.723	2.692

Notes: Blank = below EMP detection limit. All analyses of Fe, Dy, Ho, Er, Yb, and U are below detection limit and   therefore not included.

Table 4 A. Representative electron microprobe analyses of the fluorbritholite

contents (up to ca. 19 wt.%) is strictly related to the open apatite structure and its chemistry that provide the opportunity for various substitutions, resulting in possible incorporation of half the periodic chart in the atomic arrangement (Hughes and Rakovan 2002). The substitution of REEs for Ca in fluorapatite is charge-compensated by Na and Si via the coupled substitutions $REE^{3+} + Si^{4+} = Ca^{2+} + P^{5+}$ and $Na^+ + REE^{3+} = 2Ca^{2+}$ (cf. Fleet *et al.* 2000; Pan and Fleet 2002). The bulk rock composition (Table 2) indicates that the melt from which fluorapatite crystallized was a silica-undersaturated (60.2 wt.% SiO_2 with 19.5 wt.% of nepheline following CIPW norm) and significantly Na-enriched (12.11 wt.% Na_2O) comparing to the low Ca concentration (0.37 wt.% CaO). A recent experimental study documented monazite dissolution in the presence of a ($Na_2Si_2O_5$ +

H_2O) fluid, and the formation of fluorapatite-britholite solid solution (Budzyń *et al*. 2011). Experimentally reproduced high Na activity conditions partially support the interpretation in this study that an alkali-rich system promotes incorporation of REEs into primary igneous fluorapatite and fluorbritholite rather than crystallization of monazite as a primary phosphate REE-host. The light REEs (LREEs) are preferentially substituted into the structure over heavy REEs (HREEs), which are below detection limits of the electron microprobe in both fluorapatite and fluorbritholite-(Ce) (Tables 3, 4). The high LREE/HREE ratio is strictly related to the bulk-rock composition, where LREEs significantly dominate over HREEs (Table 2).

The patchy zoning in both the fluorapatite and fluorbritholite-(Ce) are typical results of metaso-

MAGDALENA DUMAŃSKA-SŁOWIK *ET AL.*

	Dark domains											
Analysis	2	5	10	11	12	15	16	17	18	20	23	24
P_2O_5	4.16	3.76	4.51	4.18	4.18	4.59	5.08	4.09	4.11	4.07	4.30	4.33
SiO_2	19.32	19.49	18.96	19.17	19.34	19.03	18.58	18.99	18.92	19.03	19.01	18.97
ThO_2	1.21	0.90	1.18	1.09	1.20	1.35	0.77	1.13	1.15	1.23	1.35	1.47
Y_2O_3	3.44	3.31	1.44	1.82	3.14	1.37	2.15	1.49	1.54	1.61	1.43	1.72
La_2O_3	11.60	11.41	10.62	11.14	11.65	10.91	10.83	10.83	11.17	11.56	10.84	10.65
Ce_2O_3	24.39	24.62	25.43	25.61	24.84	25.65	25.16	25.94	25.67	25.62	25.92	25.80
Pr_2O_3	2.80	1.88	2.93	2.65	2.28	2.98	2.69	3.04	2.74	3.05	2.30	2.95
Nd_2O_3	9.62	10.15	10.84	10.49	9.34	11.36	10.29	10.52	10.88	9.93	10.71	11.22
Sm_2O_3	1.34	1.81	1.86	1.40	1.37	1.47	1.55	1.35	1.74	1.68	1.22	1.58
Gd_2O_3	0.94	1.51	0.70	1.16	1.34	0.97	0.94	0.93	1.23	0.94	0.96	1.26
CaO	16.02	15.78	16.28	16.24	15.94	16.40	17.26	16.15	16.00	15.87	16.41	16.43
MnO	0.35	0.36	0.38	0.28	0.36	0.41	0.25	0.35	0.35	0.32	0.39	0.35
SrO												
Na_2O						0.07			0.06			
F	1.50	1.27	1.80	1.42	1.42	1.46	1.40	1.30	1.45	1.33	1.32	1.35
Cl												
H_2O	0.47	0.57	0.33	0.50	0.51	0.50	0.53	0.55	0.48	0.54	0.55	0.55
Sum	97.16	96.81	97.24	97.13	96.92	98.52	97.47	96.65	97.48	96.78	96.71	98.60
-O=(F+Cl)	0.63	0.53	0.76	0.60	0.60	0.61	0.59	0.55	0.61	0.56	0.56	0.57
total	96.53	96.27	96.49	96.53	96.33	97.91	96.88	96.11	96.87	96.22	96.15	98.03
REE_2O_3	54.13	54.69	53.81	54.27	53.97	54.71	53.60	54.10	54.96	54.40	53.38	55.16
P	0.448	0.409	0.485	0.453	0.452	0.491	0.543	0.447	0.448	0.446	0.468	0.466
Si	2.458	2.506	2.411	2.455	2.468	2.406	2.347	2.455	2.433	2.459	2.443	2.412
Th	0.035	0.026	0.034	0.032	0.035	0.039	0.022	0.033	0.034	0.036	0.039	0.042
Y	0.233	0.227	0.097	0.124	0.214	0.092	0.144	0.103	0.105	0.111	0.098	0.116
La	0.544	0.541	0.498	0.526	0.548	0.509	0.504	0.516	0.530	0.551	0.514	0.499
Ce	1.136	1.159	1.184	1.201	1.160	1.187	1.163	1.228	1.209	1.212	1.220	1.201
Pr	0.130	0.088	0.136	0.124	0.106	0.137	0.124	0.143	0.128	0.143	0.107	0.136
Nd	0.437	0.466	0.492	0.480	0.426	0.513	0.464	0.485	0.500	0.458	0.492	0.509
Sm	0.059	0.080	0.081	0.062	0.060	0.064	0.067	0.060	0.077	0.075	0.054	0.069
Gd	0.039	0.064	0.029	0.049	0.057	0.041	0.039	0.040	0.053	0.040	0.041	0.053
Ca	2.184	2.174	2.217	2.228	2.180	2.221	2.335	2.236	2.204	2.197	2.260	2.237
Mn	0.038	0.039	0.041	0.030	0.039	0.044	0.027	0.038	0.038	0.034	0.042	0.038
Sr												
Na						0.017			0.016			
F	0.604	0.516	0.723	0.575	0.571	0.582	0.560	0.530	0.590	0.544	0.537	0.544
Cl	0.000	0.000	0.000	0.000	0.000	0.000	0.000	0.000	0.000	0.000	0.000	0.000
OH	0.399	0.489	0.280	0.427	0.434	0.422	0.446	0.474	0.412	0.466	0.472	0.466
Total cations	7.742	7.780	7.705	7.762	7.745	7.762	7.780	7.786	7.773	7.764	7.780	7.779
REE	2.579	2.626	2.517	2.565	2.571	2.543	2.506	2.575	2.601	2.591	2.526	2.584

Notes: Blank = below EMP detection limit. All analyses of Fe, Dy, Ho, Er, Yb, and U are below detection limit and therefore not included.

Table 4 B. Representative electron microprobe analyses of the fluorbritholite

matic alteration leading to partial replacement via fluid-mediated coupled dissolution-reprecipitation (e.g. Putnis 2002, 2009). The reactive fluid generally operates as a catalyst, leading to the replacement of a mineral phase by a new composition of the same phase or by a completely new phase (Harlov *et al.* 2011). Chemical alteration via fluid-aided dissolution-reprecipitation may lead to the formation of various textures, including patchy zoning, but also concentric zoning that may be interpreted as a typical growth texture instead of a result of partial replacement (cf. Hetherington *et al.* 2010; Budzyń *et al.* 2011; Harlov *et al.* 2011; Williams *et al.* 2011). The process requires the same rates of dissolution of the primary phase and reprecipitation of the altered (or new) phase, which are in direct contact, separated only by a thin fluid film operating at a submicron scale to transport material across the reaction front (Harlov *et al.* 2011).

The fluorapatite showing patchy zoning and overgrowth-like rims that are bright in BSE images (Textfig. 2c) is interpreted as a primary igneous phase metasomatically altered via fluid-aided dissolution-reprecipitation. There is no doubt that the patchy zoning is the result of such a process. Although bright rims potentially may be overgrowths, the partial penetration into the grain cores along the patches borders and the presence of secondary parisite inclusions indicate that the rims were also formed by the chemical alteration of fluorapatite. The high-Na bulk composition promoted the REEs transported across fluid front penetrating fluorapatite to be incorporated into the structure via the substitution $Na^+ + REE^{3+} = 2Ca^{2+}$. The Ca (and F) released from the altered fluorapatite formed parisite

| | Fluorbritholite associated with fluorapatite | | | | | | | | | | | |
| | Dark domains | | | | | | Bright domains | | | | | |
Analysis	1	2	6	10	11	12	3	4	5	7	8	9
P_2O_5	1.79	1.80	2.66	2.21	1.80	1.78	2.21	2.71	2.53	3.20	3.35	2.62
SiO_2	19.24	19.57	18.61	19.69	19.51	19.60	18.50	18.37	18.41	17.99	18.46	18.24
ThO_2	0.86	1.03	0.82	0.83	0.84	0.77	1.01	0.91	0.98	0.94	1.00	1.05
Y_2O_3	1.63	1.66	1.48	1.41	1.68	1.66	1.81	1.61	1.50	1.66	1.54	1.65
La_2O_3	12.92	12.93	12.13	12.65	13.08	12.96	12.82	11.94	12.16	12.22	12.29	13.15
Ce_2O_3	27.86	27.97	27.77	28.43	27.72	27.94	28.07	28.85	28.32	28.15	27.92	27.80
Pr_2O_3	3.03	2.82	3.07	2.54	2.39	2.60	2.83	2.39	2.93	2.90	2.86	2.54
Nd_2O_3	10.65	10.47	11.58	11.15	10.90	10.88	11.85	11.70	11.49	12.23	11.29	11.28
Sm_2O_3	1.61	1.67	1.54	1.58	1.74	1.55	1.72	1.72	1.21	1.51	1.69	1.16
Gd_2O_3	1.19	1.06	1.01	0.86	1.43	1.16	1.08	1.23	0.65	1.02	1.63	1.25
CaO	10.68	10.75	11.33	11.37	9.98	10.07	7.97	9.04	9.24	9.10	9.53	8.46
MnO	0.52	0.50	0.60	0.60	0.68	0.72	0.59	0.64	0.62	0.51	0.59	0.52
SrO		0.13	0.07	0.12	0.13	0.12		0.15	0.08			0.07
NaO	0.42	0.41	0.32	0.33	0.51	0.46	0.74	0.45	0.63	0.53	0.51	0.54
F	2.36	2.18	1.95	1.48	2.09	2.31	1.68	1.35	1.79	1.40	1.50	1.56
Cl			0.06				0.07		0.07	0.07		
H_2O	0.00	0.00	0.00	0.00	0.00	0.00	0.00	0.00	0.00	0.00	0.00	0.00
Sum	94.75	94.95	95.01	95.23	94.48	94.56	92.96	93.05	92.59	93.42	94.17	91.88
-O=(F+Cl)	0.99	0.92	0.83	0.63	0.88	0.97	0.72	0.57	0.77	0.60	0.63	0.66
total	93.76	94.03	94.17	94.60	93.60	93.59	92.24	92.48	91.83	92.82	93.54	91.22
REE_2O_3	58.88	58.58	58.58	58.62	58.94	58.73	60.19	59.43	58.26	59.69	59.23	58.83

Notes: Blank = below EMP detection limit. All analyses of Fe, Dy, Ho, Er, Yb and U are below detection limit and therefore not included.

Table 4 C. Representative electron microprobe analyses of the fluorbritholite

inclusion, which points to the presence of a CO_2 component in the reactive fluid. The source of REEs was probably the fluorbritholite-(Ce) that also shows patchy zoning, although the brighter domains concentrate near the cores, whilst darker domains, interpreted as chemically altered, are present near the rims. The reactive fluid penetrating the primary igneous britholite-(Ce) released REEs that were mobilized and incorporated into the altered fluorapatite. REEs mobility was induced by a fluid with a high F activity (cf. Pan and Fleet 1996; Tropper and Manning 2007).

The progress of the alteration differed significantly, depending on the distance between the fluorapatite and fluorbritholite-(Ce) grains in the host mariupolite. The close proximity of fluorbritholite-(Ce) resulted in the fluid-aided dissolution-reprecipitation replacement of the altered fluorapatite by secondary monazite and fluorite that form symplectite-like grains surrounding, and present within, the fluorapatite. The altered fluorbritholite-(Ce) was a source of REEs that were mobilized and transported over a short distance to the altered fluorapatite to form monazite. Mobilization of PO_4^{3-} anions from the fluorapatite in the presence of F-rich fluid followed, with mobilization of Ca^{2+} to form fluorite. Additionally, the altered domains in fluorbritholite-(Ce) contain parisite inclusions, suggesting a CO_2 component in the reactive fluid that facilitated chemical alteration.

There is no direct evidence as to the precise conditions of fluorapatite and fluorbritholite-(Ce) alteration. The presence of secondary monazite with a low Th content may suggest low temperature conditions, according to the previous work that has documented very low Th contents in monazite formed during low-grade metamorphism (Rasmussen and Muhling 2009) or hydrothermal events (Kempe et al. 2008). However, the Th concentration in the monazite is also controlled by the Th budget in the bulk composition during monazite crystallization. Here, the ThO_2 content in monazite (0.5–1.2 wt.%) is similar to that in the fluorbritholite-(Ce) (0.5–1.5 wt.%), and there is no other potential source among the primary mineral phases.

A recent experimental study on the stability relationships between monazite, fluorapatite, allanite and REE-epidote (Budzyń et al. 2011), even though it concerned a silica-saturated system, may be a reference point in this discussion. The experimental results from runs with NaOH (alkaline) fluid showed that starting monazite is dissolved to form secondary monazite and fluorapatite-britholite at lower P-T conditions (450°C, 450 MPa), while increasing P or T promotes dissolution of monazite to form secondary fluorapatite (500°C, 450 MPa) or fluorapatite-britholite phase and allanite (450°C, 610-580 MPa) (Budzyń et al. 2011). Because the Ca activity plays a significant role in the stability relations of monazite, allanite and fluorapatite in granitic rocks (Lee and Dodge 1964; Lee and Bastron 1967; Bea 1996; Broska et al. 2000; Claeson 2002), it is unexpected that allanite or REE-epidote would form in the mariupolite, which has a low Ca content. Rather, high temperature conditions promoted crystallization of primary REE-enriched fluorapatite
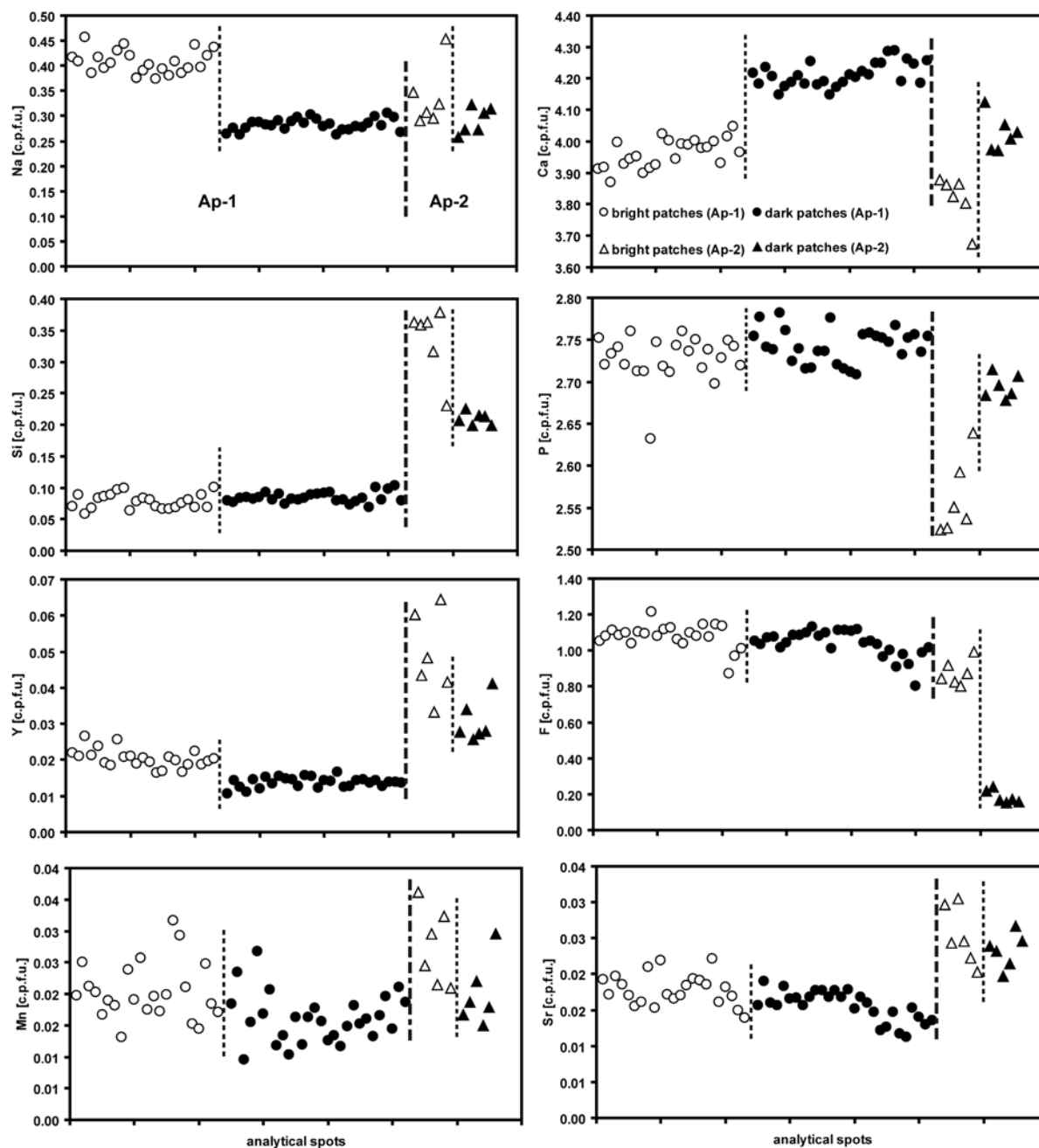
Text-fig. 6 A. Plots showing compositional variations between dark and bright domains in (Ap-1) the fluorapatite present as individual grains; and (Ap-2) the fluorapatite in contact with the fluorbritholite shown in Figure 5. The cations are calculated on the basis of 13 O atoms

and fluorbritholite from the parent magma, whilst late- to post-magmatic metasomatic alteration promoted formation of monazite stable under low-temperature conditions.

CONCLUSIONS

The mechanism of the fluid-mediated coupled dissolution-reprecipitation that promoted alteration of the primary igneous fluorapatite and fluorbritholite-(Ce) in the mariupolite significantly depended on the distance between the phases in the host rock. The altered domains in the individual fluorapatite or fluorbritholite-(Ce) grains were replaced by the same phases with a new composition. The REEs were mobilized from the altered fluorbritholite-(Ce) and transported by a fluid with high F activity. The

STABILITY RELATIONSHIPS OF REE-BEARING PHOSPHATES IN AN ALKALI-RICH SYSTEM
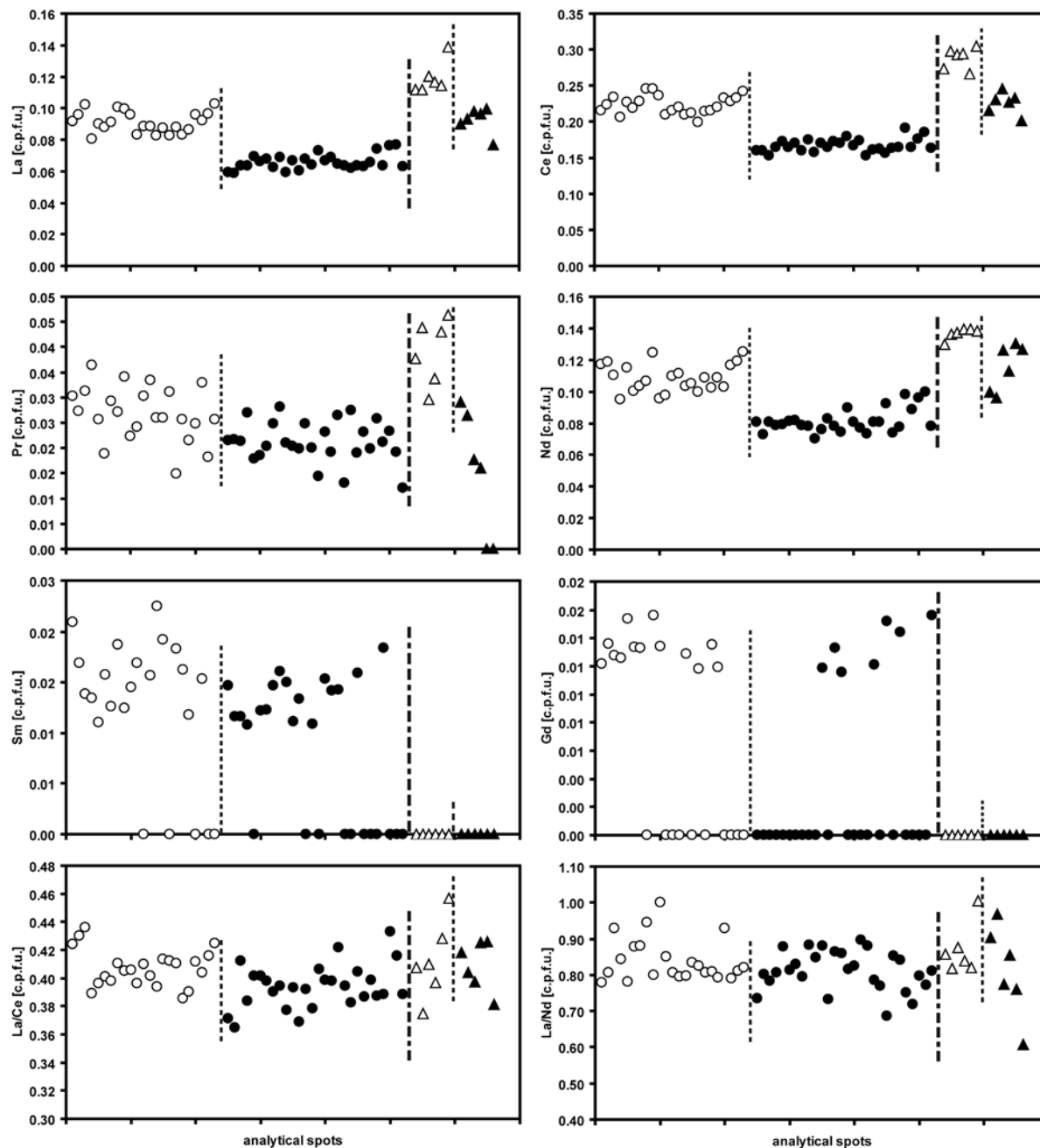
Text-fig. 6 B. Plots showing compositional variations between dark and bright domains in (Ap-1) the fluorapatite present as individual grains; and (Ap-2) the fluorapatite in contact with the fluorbritholite shown in Figure 5. The cations are calculated on the basis of 13 O atoms

Text-fig. 7. Plot of formula proportions (Y + REE + P) vs. (Th + Si) calculated on the basis of 4 O atoms for the monazite from the mariupolite. Dashed lines represent the huttonitic substitution $(Th,U)SiREE_{-1}P_{-1}$ and cheralitic substitution $Ca(Th,U)REE_{-2}$ (Förster 1998; Linthout 2007)

262
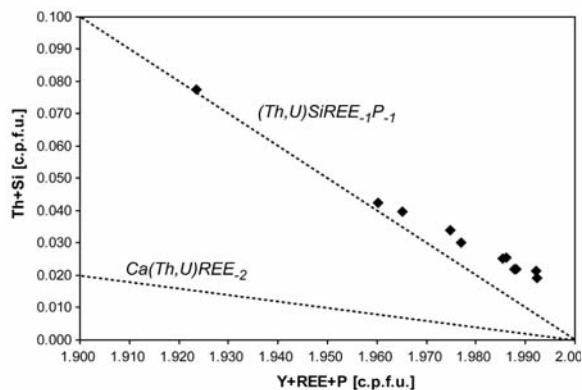
	1	2	3	5	6	7	8	9	10	11
P_2O_5	28.90	28.93	28.70	29.06	29.06	28.67	28.78	28.92	28.79	29.11
SiO_2	0.43	0.58	0.49	0.49	0.37	0.38	0.58	0.67	0.65	0.41
ThO_2	0.45	0.78	0.58	0.63	0.49	0.72	1.17	1.64	1.44	0.62
Y_2O_3	0.11	0.08	0.13	0.11			0.09			
La_2O_3	14.63	15.24	14.74	14.83	16.34	16.90	16.81	21.58	21.67	16.82
Ce_2O_3	34.08	34.08	33.93	33.87	35.23	35.03	34.67	34.99	34.87	35.18
Pr_2O_3	3.96	3.97	3.92	3.98	3.79	3.76	3.63	2.95	3.15	3.60
Nd_2O_3	14.11	13.70	13.89	13.85	12.88	12.15	12.27	8.36	8.52	12.52
Sm_2O_3	1.85	1.71	1.85	1.83	1.38	1.28	1.23			1.21
Gd_2O_3	0.88		0.73	0.98						
CaO	0.09	0.23	0.25	0.10	0.06	0.21	0.13	0.03	0.03	0.03
total	99.48	99.30	99.21	99.72	99.60	99.10	99.35	99.13	99.13	99.49
Cations per formula unit on the basis of 4 oxygens										
P	0.965	0.965	0.961	0.966	0.971	0.966	0.964	0.973	0.971	0.972
Si	0.017	0.023	0.020	0.019	0.014	0.015	0.023	0.027	0.026	0.016
Th	0.004	0.007	0.006	0.006	0.005	0.007	0.011	0.016	0.014	0.006
Y	0.002	0.002	0.003	0.002			0.002			
La	0.213	0.221	0.215	0.215	0.238	0.248	0.245	0.316	0.318	0.245
Ce	0.492	0.491	0.491	0.487	0.509	0.510	0.502	0.509	0.509	0.508
Pr	0.057	0.057	0.056	0.057	0.054	0.055	0.052	0.043	0.046	0.052
Nd	0.199	0.193	0.196	0.194	0.181	0.173	0.173	0.119	0.121	0.176
Sm	0.053	0.049	0.053	0.052	0.039	0.037	0.035			0.035
Gd	0.012		0.010	0.013						
Ca	0.004	0.010	0.011	0.004	0.003	0.009	0.005	0.001	0.001	0.001
total	2.017	2.017	2.021	2.015	2.014	2.019	2.014	2.004	2.006	2.012
REE	1.027	1.013	1.024	1.020	1.022	1.022	1.010	0.987	0.994	1.016
Ce/La	2.313	2.219	2.285	2.267	2.141	2.058	2.047	1.609	1.597	2.076
Ce/Nd	2.475	2.549	2.505	2.506	2.805	2.957	2.897	4.292	4.194	2.881
Nd/La	0.934	0.870	0.912	0.904	0.763	0.696	0.707	0.375	0.381	0.720

Notes: Blank = below EMP detection limit.
Analyses of Tb, Dy, Ho, Er, Yb, U, Pb and S are below detection limit and therefore not included.

Table 5. Representative electron microprobe analyses of the secondary monazite

short distance of element transport between the contacting fluorapatite and fluorbritholite-(Ce) in contact has resulted in a partial replacement of the fluorapatite by secondary phosphate REE-host, monazite and also fluorite due to the release of Ca component from the altered primary phases. Additionally, the secondary parisite formed in the altered domains of the fluorapatite and fluorbritholite-(Ce) as a result of this alkali-bearing fluid induced process. The metasomatic alterations proceeded in the presence of the fluid with high F, Na and CO_2 activity during a late- to post-magmatic low-temperature hydrothermal event.

Acknowledgements

REFERENCES

Bea, F. 1996. Residence of REE, Y, Th and U in granites and crustal protoliths; Implications for the chemistry of crustal melts. *Journal of Petrology*, **37** (3), 521–552.

Berger, A., Gnos, E., Janots, E., Fernandez, A. and Giese, J. 2008. Formation and composition of rhabdophane, bastnäsite and hydrated thorium minerals during alteration: Implications for geochronology and low-temperature processes. *Chemical Geology*, **254**, 238–248.

Bingen, B., Demaiffe, D. and Hertogen, J. 1996. Redistribution of rare earth elements, thorium, and uranium over accessory minerals in the course of amphibolite to granulite facies metamorphism: The role of apatite and monazite in orthogneisses from southwestern Norway. *Geochimica et Cosmochimica Acta*, **60** (8), 1341–1354

Broska, I. and Siman, P. 1998. The breakdown of monazite in the West-Carpathian Veporic orthogneisses and Tatric granites. *Geologica Carpathica*, **49**, 161–167.

Broska, I., Petrík, I. and Williams, C.T. 2000. Coexisting monazite and allanite in peraluminous granitoids of the Tribec Mountains, Western Carpathians. *American Mineralogist*, **85**, 22–32

Broska, I., Williams, C.T., Janák, M. and Nagy, G. 2005. Alteration and breakdown of xenotime-(Y) and monazite-

(Ce) in granitic rocks of the Western Carpathians, Slovakia. *Lithos*, **82**, 71–83.

Budzyń, B., Hetherington, C.J., Williams, M.L., Jercinovic, M.J. and Michalik, M. 2010. Fluid-mineral interactions and constraints on monazite alterations during metamorphism. *Mineralogical Magazine*, **74** (4), 633–655

Budzyń B., Harlov D.E., Williams M.L. and Jercinovic M.J. 2011. Experimental determination of stability relations between monazite, fluorapatite, allanite, and REE-epidote as a function of pressure, temperature, and fluid composition. *American Mineralogist*, **96**, 1547–1567.

Claeson, D.T. 2002. Stability of REE-bearing minerals in a metaluminous leucotonalite from the Eriksberg gabbro, Transscandinavian Igneous Belt, Sweden. *Neues Jahrbuch für Mineralogie, Abhandlungen*, **177** (3), 277–291.

Donskoy, A.N. 1982. The nepheline complex of alkaline Oktyabr'skii massif, pp. 1–150. The Ukrainian Academy of Science, Kiev. [In Ukrainian]

Dumańska-Słowik, M. Sikorska, M. and Heflik, W. 2011a. Dissolved-recrystallized zircon from mariupolite in the Mariupol Massif, Priazovje (SE Ukraine). *Acta Geologica Polonica*, **61** (3), 277–288.

Dumańska-Słowik, M., Baranov, P, Heflik, W., Natkaniec-Nowak, L., Shevchenko, S. and Tsotsko, L.I. 2011b. Mariupolites of the Oktyabrsky Massif (SE Ukraine) – a less known rocks in the gemstone trade. *Zeitschrift der Deutschen Gemmologischen Gesellschaft*, **60**, 37–48.

Finger, F., Broska, I., Roberts, M.P. and Schermaier, A. 1998. Replacement of primary monazite by apatite-allanite-epidote coronas in an amphibolite facies granite gneiss from the eastern Alps. *American Mineralogist*, **83**, 248–258.

Finger, F. and Krenn, E. 2007. Three metamorphic monazite generations in a high-pressure rock from the Bohemian Massif and the potentially important role of apatite in stimulating polyphase monazite growth along a PT loop. *Lithos*, **95**, 103–115.

Fleet, M.E., Liu, X. and Pan, Y. 2000. Rare-earth elements in chlorapatite [$Ca_{10}(PO_4)6Cl_2$]: Uptake, site preference, and degradation of monoclinic structure. *American Mineralogist*, **85**, 1437–1446.

Harlov, D.E., Förster, H.J. and Schmidt, C. 2003. High P–T experimental metasomatism of a fluoroapatite with significant britholite and fluorellesadite components: implications for LREE mobility during granulite-facies metamorphism. *Mineralogical Magazine*, **67** (1), 61–72.

Harlov, D.E. and Förster, H.J. 2003. Fluid-induced nucleation of (Y+REE)-phosphate minerals within apatite: Nature and experiment. Part II. Fluorapatite. *American Mineralogist*, **88**, 1209–1229.

Harlov, D.E., Wirth R. and Förster, H.J. 2005. An experimental study of dissolution-reprecipitation in fluoroapatite: fluid infiltration and the formation of monazite.

Contributions to Mineralogy and Petrology, **150**, 268–286.

Harlov, D.E., Marschall, H.R. and Hanel, M. 2007. Fluorapatite-monazite relationships in granulite-facies metapelites, Schwarzwald, southwest Germany. *Mineralogical Magazine*, **71** (2), 223–234.

Harlov, D.E., Wirth, R. and Hetherington, C.J. 2011. Fluid-mediated partial alteration in monazite: the role of coupled dissolution-reprecipitation in element redistribution and mass transfer. *Contributions to Mineralogy and Petrology*, **162**, 329–348.

Harlov, D.E. and Wirth, R. 2012. Experimental incorporation of Th into xenotime at middle to lower crustal *P-T* utilizing alkali-bearing fluids. *American Mineralogist*, **97**, 641–652.

Hetherington, C.J. and Harlov, D.E. 2008. Metasomatic thorite and uraninite inclusions in xenotime and monazite from granitic pegmatites, Hidra anorthosite massif, southwestern Norway: Mechanics and fluid chemistry. *American Mineralogist*, **93**, 806–820.

Hetherington, C.J., Harlov, D.E. and Budzyń, B. 2010. Experimental metasomatism of monazite and xenotime: mineral stability, REE mobility and fluid composition. *Mineralogy and Petrology*, **99** (3–4), 165–184

Hughes, J.M. and Rakovan, J. 2002. The Crystal Structure of Apatite, $Ca_5(PO_4)_3(F,OH,Cl)$. In: M.J. Kohn, J. Rakovan and J.M. Hughes (Eds), Phosphates – Geochemical, Geological and Materials Importance. *Reviews in Mineralogy and Geochemistry*, **48**, 1–12.

Janots, E., Negro, F., Brunet, F., Goffé, B., Engi, M. and Bouybaouène, M.L. 2006. Evolution of the REE mineralogy in HP–LT metapelites of the Sebtide complex, Rif, Morocco: Monazite stability and geochronology. *Lithos*, **87**, 214–234.

Janots, E., Engi, M., Berger, A., Allaz, J., Schwarz, J.-O. and Spandler, C. 2008. Prograde metamorphic sequence of REE minerals in pelitic rocks of the Central Alps: implications for allanite–monazite–xenotime phase relations from 250 to 610°C. *Journal of Metamorphic Geology*, **26** (5), 509–526.

Janots, E., Berger, A. and Engi, M., 2011. Physico-chemical control on the REE minerals in chloritoid-grade metasediments from a single outcrop (Central Alps, Switzerland). *Lithos*, **121**, 1–11.

Kempe, U., Lehmann, B., Wolf, D., Rodionov, N., Bombach, K., Schwengfelder, U. and Dietrich, A. 2008. U-Pb SHRIMP geochronology of Th-poor, hydrothermal monazite: An example from the Llallagua tin-porphyry deposit, Bolivia. *Geochimica et Cosmochimica Acta*, **72**, 4352–4366.

Krenn, E. and Finger, F. 2007. Formation of monazite and rhabdophane at the expense of allanite during Alpine low temperature retrogression of metapelitic basement rocks

from Crete, Greece: Microprobe data and geochronological implications. *Lithos*, **95**, 130–147

Krivdik, S.G., Nivin, V.A., Kul'chitskaya, A.A., Voznak, D.K., Kalinichenko, A.M., Zagnitko, V.N. and Dubyna, A.V. 2007. Hydrocarbons and other volatile components in alkaline rocks from the Ukrainian Shield and Kola Penisula. *Geochemistry International*, **45** (3), 270–294.

Lee, D.E. and Dodge, F.C.W. 1964. Accessory minerals in some granitic rocks in California and Nevada as a function of calcium content. *American Mineralogist*, **49**, 1660–1669.

Lee, D.E. and Bastron, H. 1967. Fractionation of rare-earth elements in allanite and monazite as related to geology of the Mt. Wheeler mine area, Nevada. *Geochimica et Cosmochimica Acta*, **31**, 339–356.

Morozewicz, J. 1902. Über Mariupolit, ein extremes Glied der Elaeolithsyenite. *Tschermaks Mineralogische und Petrographische Mitteilungen* **21**, 238–246.

Morozewicz, J. 1929. Mariupolite and its relatives. *Prace Polskiego Instytutu Geologicznego* **2** (3), p. 130. [In Polish]

Ondrejka, M., Uher, P., Putiš, M., Broska, I., Bačík, P., Konečný, P. and Schmidt, I. 2012. Two-stage breakdown of monazite by post-magmatic and metamorphic fluids: An example from the Veporic orthogneiss, Western Carpathians, Slovakia. *Lithos*, doi: 10.1016/j.lithos. 2012.03.012

Pan, Y. and Fleet, M.E. 1996. Rare element mobility during prograde granulite facies metamorphism: significance of fluorine. *Contributions to Mineralogy and Petrology*, **123**, 251–262.

Pan, Yu. and Fleet, M. 2002. Compositions of apatite-group minerals: substitution mechanisms and controlling factors. In: M.J. Kohn, J. Rakovan, J.M. Hughes (Eds), Phosphates – Geochemical, Geological and Materials Importance. *Reviews in Mineralogy and Geochemistry*, **48**, 13–49.

Piccoli, P.M. and Candela, P.A. 2002. Apatite in igneous systems. In: M.J. Kohn, J. Rakovan, J.M. Hughes (Eds), Phosphates – Geochemical, Geological and Materials Importance. *Reviews in Mineralogy and Geochemistry*, **48**, 255–292.

Pouchou, I. L. and Pichoir, F. 1985. "PAP" (phi-rho-z) procedure for improved quantitative microanalysis. In: I.T. Armstrong (Ed.), Microbeam Analysis, pp. 104–106. San Francisco Press; San Francisco.

Putnis, A. 2002. Mineral replacement reactions: from macroscopic observations to microscopic mechanisms. *Mineralogical Magazine*, **66**, 689–708.

Putnis, A. 2009. Mineral replacement reactions. In: E.H. Oelkers and J. Schott (Eds), Thermodynamics and Kinetics of Water-Rock Interaction. *Reviews in Mineralogy and Geochemistry*, **70**, 87–124.

Rasmussen, B. and Muhling, J.R. 2009. Reactions destroying detrital monazite in greenschist-facies sandstones from the Witwatersrand basin, South Africa. *Chemical Geology*, **264**, 311–327.

Read, D., Andreoli, M.A.G., Knoper, M., Williams, C.T. and Jarvis, N. 2002. The degradation of monazite: Implications for the mobility of rare-earth and actinide elements during low-temperature alteration. *European Journal of Mineralogy*, **14**, 487–498.

Rønsbo, J.G. 1989. Coupled substitution involving REEs and Na and Si in apatites in alkaline rocks from the Llimaussag intrusion, South Greenland, and the petrological implications. *American Mineralogist*, **74**, 896–901.

Rønsbo, J.G. 2008. Apatite in the Llimaussag alkaline complex: Occurrence, zonation and compositional variation. *Lithos*, **106**, 71–82.

Seydoux-Guillaume, A.M., Paquette, J.L., Wiedenbeck, M., Montel, J.M., and Heinrich, W. (2002a) Experimental resetting of the U-Th-Pb systems in monazite. *Chemical Geology*, **191**, 165–181.

Sharygin, V.V., Krivdik, S.G., Pospelova, L.N. and Dubina, A.V. 2009. Zn-kupletskite and hendricksite in the agpaitic phonolites of the Oktyabrskii Massif, Azov Region, Ukraine. *Doklady Earth Sciences*, **425A** (3), 499–504.

Solodov, N.A. 1985. The mineralo-genesis of rare metal formations, pp. 1–225. Niedra. [In Ukrainian]

Spear, F.S. 2010. Monazite–allanite phase relations in metapelites. *Chemical Geology*, **279**, 55–62.

Teufel, S. and Heinrich, W. 1997. Partial resetting of the U-Pb isotope system in monazite through hydrothermal experiments: An SEM and U-Pb isotope study. *Chemical Geology*, **137**, 273–281.

Tichonienkova, R.J, Osokin, J.D. and Gonzjejev, A.A. 1967. Rare-metals metasomatites of alkaline massives, pp. 1–196. Nauka. [In Ukrainian]

Tropper, P. and Manning, C.E. 2007. The solubility of fluorite in H_2O and H_2O–NaCl at high pressure and temperature. *Chemical Geology*, **242**, 199–306.

Tomkins, H.S. and Pattison, D.R.M. 2007. Accessory phase petrogenesis in relation to major phase assemblages in pelites from the Nelson contact aureole, southern British Columbia. *Journal of Metamorphic Geology*, **25**, 401–421.

Upadhyay, D. and Pruseth, K.L. 2012. Fluid-induced dissolution breakdown of monazite from Tso Morari complex, NW Himalayas: evidence for immobility of trace elements. *Contributions to Mineralogy and Petrology*, doi: 10.1007/s00410-012-0739-3.

Williams, M.L., Jercinovic, M.J., Harlov, D.E., Budzyń, B. and Hetherington, C.J. 2011. Resetting monazite ages during fluid-related alteration. *Chemical Geology*, **283**, 218–225.

Wing, B., Ferry, J.M. and Harrison, T.M. 2003. Prograde destruction and formation of monazite and allanite during contact and regional metamorphism of pelites: petrology and geochronology. *Contributions to Mineralogy and Petrology*, **145**, 228–250

Volkova, T.P. 2000. The genesis and ore mineralization of alkaline rocks from the Oktyabr'skii Massif. *Sbornik nauchnykh trudov*, **4**, 9–10. [In Ukrainian]

Volkova, T.P. 2001. The productivity criterion of REE and ore mineralization within rocks of the Oktyabr'skii Massif *Naukovi praci DonDTU.*, **36**, 63–69. [In Ukrainian]